

# Interferometric fluorescent super-resolution microscopy resolves 3D cellular ultrastructure

Gleb Shtengel<sup>a</sup>, James A. Galbraith<sup>b</sup>, Catherine G. Galbraith<sup>c</sup>, Jennifer Lippincott-Schwartz<sup>d,1</sup>, Jennifer M. Gillette<sup>d</sup>, Suliana Manley<sup>d</sup>, Rachid Sougrat<sup>d</sup>, Clare M. Waterman<sup>e</sup>, Pakorn Kanchanawong<sup>e</sup>, Michael W. Davidson<sup>f</sup>, Richard D. Fetter<sup>a</sup>, and Harald F. Hess<sup>a,1</sup>

<sup>a</sup>Howard Hughes Medical Institute, Janelia Farm Research Campus, Ashburn, VA 20147; <sup>b</sup>National Institute of Neurological Disorders and Stroke; <sup>c</sup>National Institute of Dental and Craniofacial Research; <sup>d</sup>Cell Biology and Metabolism Branch, National Institute of Child Health and Human Development; and <sup>e</sup>Laboratory of Cell and Tissue Morphodynamics, National Heart Lung and Blood Institute, National Institutes of Health, Bethesda, MD 20892; and <sup>f</sup>National High Magnetic Field Laboratory and Department of Biological Sciences, Florida State University, Tallahassee, FL 32310

Contributed by Jennifer Lippincott-Schwartz, December 25, 2008 (sent for review November 19, 2008)

**Understanding molecular-scale architecture of cells requires determination of 3D locations of specific proteins with accuracy matching their nanometer-length scale. Existing electron and light microscopy techniques are limited either in molecular specificity or resolution. Here, we introduce interferometric photoactivated localization microscopy (iPALM), the combination of photoactivated localization microscopy with single-photon, simultaneous multiphase interferometry that provides sub-20-nm 3D protein localization with optimal molecular specificity. We demonstrate measurement of the 25-nm microtubule diameter, resolve the dorsal and ventral plasma membranes, and visualize the arrangement of integrin receptors within endoplasmic reticulum and adhesion complexes, 3D protein organization previously resolved only by electron microscopy. iPALM thus closes the gap between electron tomography and light microscopy, enabling both molecular specification and resolution of cellular nanoarchitecture.**

fluorescence microscopy | interferometry | PALM |  
photoactivated localization microscopy | single molecule imaging

A fundamental question in biomedical research is how specific, nanometer-scale biomolecules are organized into multicomponent micron-scale structural and signaling ensembles that facilitate cell function. For example, microtubules are built of 8-nm tubulin subunits that incorporate on the ultrastructural level into polymers 25 nm in diameter and  $>10\ \mu\text{m}$  in length that serve as the building blocks of superstructures such as mitotic spindles and flagella. However, key challenges remain for determining cellular ultrastructure with high molecular specificity. Because cellular structures are organized on the nanoscale, nanometer resolution is required. Immunoelectron microscopy (EM)-based approaches provide the necessary resolution, but they lack robust molecular specificity because the large size of the antibodies hampers their penetration into dense structures and the specificity of the antibody can be compromised by cross-reactivity and epitope masking caused by the harsh fixation often used for high-resolution EM. Fluorescence microscopy coupled with fluorescent protein (FP) fusion technology enables imaging cellular structure with exquisite molecular specificity, but the resolution of 3D images is diffraction-limited to  $\approx 200\ \text{nm}$  in the lateral and  $\approx 500\ \text{nm}$  in the axial direction, limiting conventional fluorescence to the characterization of cellular superstructure. Some of the recent fluorescence-based super-resolution microscopy techniques (1–5) demonstrated a resolution of  $<100\ \text{nm}$  in the vertical direction; however, this is still insufficient to bridge the resolution gap between cellular ultrastructure and superstructure. To achieve near-ultrastructural 3D resolution even for the limited photon outputs of high-molecular-specificity FPs, we have developed a single-photon multiphase interferometric scheme and integrated it with a lateral photoactivated localization microscopy (PALM) (6),

resulting in a highly photon-efficient system called interferometric PALM (iPALM).

Quantitative high-precision positional measurements are commonly made with phase-based interferometry (7), where coherent light waves from 2 optical paths (a reference path and a measured path) are combined to create a signal that modulates on the length scale of an optical wavelength. Interferometry is widely applied to position objects to  $10^{-10}$ -meter accuracy, measure optical surfaces, and even scout for gravity waves with  $10^{-18}$ -meter sensitivity. Interferometric microscopes (8, 9) when combined with phase-shifting techniques (10) can form sub-nanometer-height images and are routinely used in industry to qualify semiconductor processing or hard disk drive head profiles. However, the benefit of such a quantitative interferometric method has so far been elusive for biological systems, despite the wealth of open questions that hinge on the 3D molecular organization at the nanometer scale. Most biological imaging applications use Nomarski differential interference contrast, Zernike phase contrast, or interference reflection microscopy, which harness qualitative interferometric contrast that depends on the refractive index variations within biological materials and forgoes the molecular specificity afforded by fluorescent labeling. Other more recent concepts, such as  $4\pi$  (11) and  $\text{I}^2\text{M}$  (12), use interference to create a more precise vertical focus (point-spread function) but do not extract explicit phase values from the interfered signal, a critical advantage that is exploited by phase-shifting techniques. One quantitative approach (13) measures the phase of a fluorescent source but requires multiple replicas of the same sample structure over a patterned silicon substrate, a very limiting requirement for bioimaging.

The obstacles to the precise measurement of biological samples by phase-shifting interferometry techniques may seem fundamental. Cells, tissues, or other biological materials typically lack single well-defined reflecting surfaces and interact with visible light weakly and with low molecular specificity. On the other hand, fluorescence provides superb molecular specificity but poses a new problem for interferometry: how to form 2 path-dependent phase coherent beams that can undergo interference. The brightness of fluorescent labels is also highly variable because of photobleaching and other photophysical

Author contributions: G.S., J.A.G., C.G.G., J.L.-S., J.M.G., S.M., R.S., C.M.W., P.K., and H.F.H. designed research; G.S., J.A.G., C.G.G., J.M.G., S.M., R.S., P.K., R.D.F., and H.F.H. performed research; G.S., J.A.G., C.G.G., J.M.G., S.M., P.K., M.W.D., and H.F.H. contributed new reagents/analytic tools; G.S., J.A.G., C.G.G., J.M.G., S.M., P.K., and H.F.H. analyzed data; and G.S., J.A.G., C.G.G., J.L.-S., J.M.G., S.M., C.M.W., P.K., M.W.D., R.D.F., and H.F.H. wrote the paper.

The authors declare no conflict of interest.

Freely available online through the PNAS open access option.

<sup>1</sup>To whom correspondence may be addressed. E-mail: hessh@janelia.hhmi.org or jlippinc@helix.nih.gov.

This article contains supporting information online at [www.pnas.org/cgi/content/full/0813131106/DCSupplemental](http://www.pnas.org/cgi/content/full/0813131106/DCSupplemental).

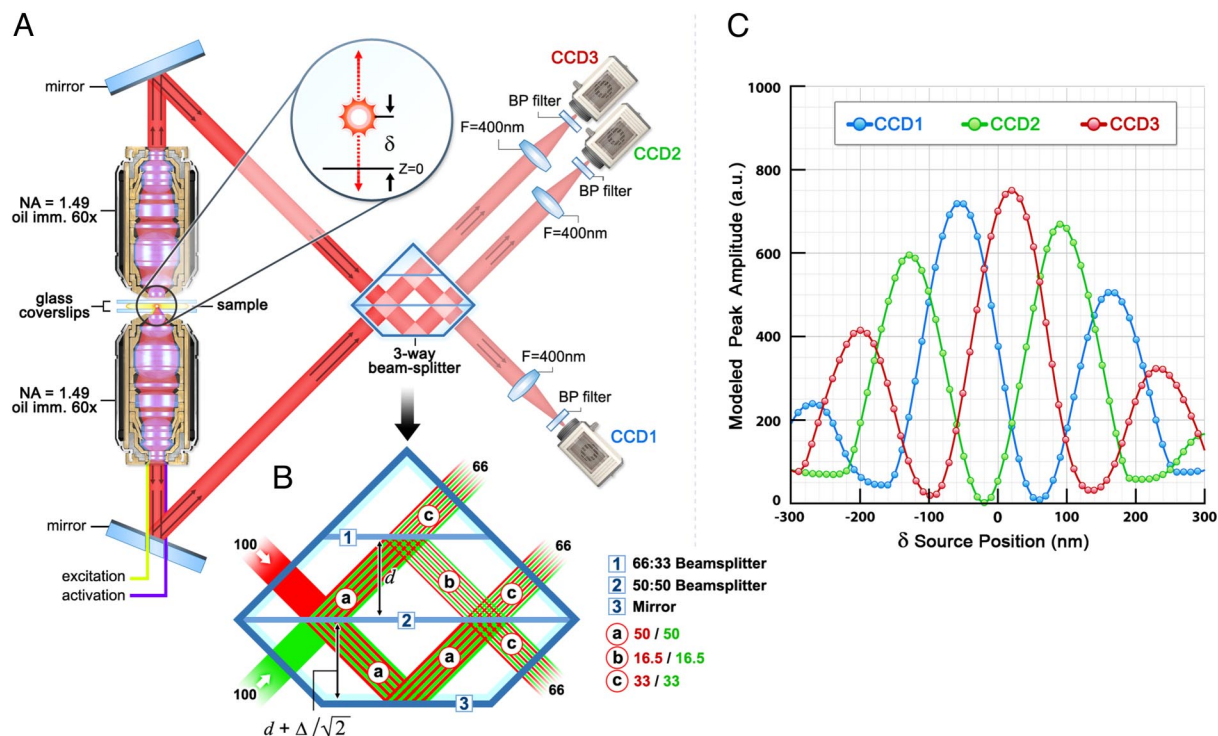


**Fig. 1.** Schematics and operating principle of multiphase interferometric microscope illustrating how Z-position is resolved. (A and B) Schematic of the single-photon multiphase fluorescence interferometer. A point source with z-position  $\delta$  emits a single photon both upwards and downwards. These 2 beams (color coded as red and green in B) interfere in a special 3-way beam splitter. (C) The self-interfered photon propagates to the 3 color-coded CCD cameras with amplitudes that oscillate  $120^\circ$  out of phase as indicated.

processes, factors that undermine the ability to take multiple sequential measurements and reliable calibrations that form the basis of phase-shift interferometry.

We have configured an optical system to overcome these obstacles using a combination of insights. First, single fluorescent molecules such as FPs are intrinsic quantum sources. Thus, wave-particle duality allows a single fluorescent photon to form its own coherent reference beam. An emitted photon can simultaneously travel 2 distinct optical paths, which are subsequently recombined so that the photon interferes with itself. The position of the emitter directly determines the difference in the path lengths, hence the relative phase between the 2 beams. This principle has been used in fluorescence interferometry (13, 14) and spectral self-interference fluorescence microscopy (15). Second, the optical system can be configured so that interference can take place over a wide range of lateral source positions to form interference images on an area array detector, such as a CCD for rapid parallel acquisition. Finally and most importantly, *simultaneous multiphase* detection must be implemented for each photon. Such detection methodology is tolerant to intensity variations and short fluorescent lifetimes; it ensures proper self-calibration, and provides complete information to extract a position-dependent interference phase angle.

## Results and Discussion

The essence of the single-photon interferometric fluorescence imaging concept is illustrated in Fig. 1, and core to this concept is a custom 3-way beam splitter. Three-way or even higher-order beam splitters are commonly used in a single-mode context (16–18) such as fiber optic gyroscopes, planar waveguide devices for telecommunications, or precision metrology of an object's position. Our device extends this multiphase interference beyond the single-mode, single-point case to the multiphase, and multiple-source case necessary for imaging biological samples. It is composed of 3

parallel planes of a 66:33 beam splitter, a 50:50 beam splitter, and a mirror (Fig. 1B). Self-interference of a single-photon source (such as a fluorescent protein in a sample) placed at the focal plane of 2 opposed objectives enables a precise determination of its axial position. Upon radiation, a fluorescent photon simultaneously enters both the upper and lower objectives, as illustrated in Fig. 1A. The difference in path lengths of the upper and lower beams directly depends on the axial position of the source. Because the photon self-interferes in the 3-way beam splitter, this position-dependent phase difference modulates the relative intensities of the 3 output beams as shown in Fig. 1C. Therefore, the axial position of the source molecule can be determined from the relative amplitudes of the source images from the 3 cameras. Localized lateral positions of a source molecule can be extracted by finding their centers from the same image set so that no extra data acquisition is needed to obtain the full 3D data coordinates. The mathematical description is presented below. The experimental validation of the performance of iPALM, as well as a tutorial demonstrating the interferometry concept are presented in [supplementing information \(SI\)](#).

The resolution capability of iPALM for determining the 3D location on the length scale of biomolecules is presented in Fig. 2. The localization accuracy of a single fluorescent source imaged repetitively for 25,000 frames is shown in Fig. 2A. Even with only 1,500 photons into a  $4\pi$  solid angle (1,200 photons detected), iPALM resolves the position of the source with full width at half maximum (FWHM) of 9.8 nm axially. The lateral position is derived from the centroid of the image spot (19) and the lateral localization accuracy of this same source has FWHM of 22.8 nm. Fig. 2B compares the dependence of localization accuracy on source brightness for iPALM compared with superresolution defocusing approaches (2, 3, 20, 21). Localization accuracy depends critically on source brightness, and scales approximately as the inverse square root of the number of photons detected. This



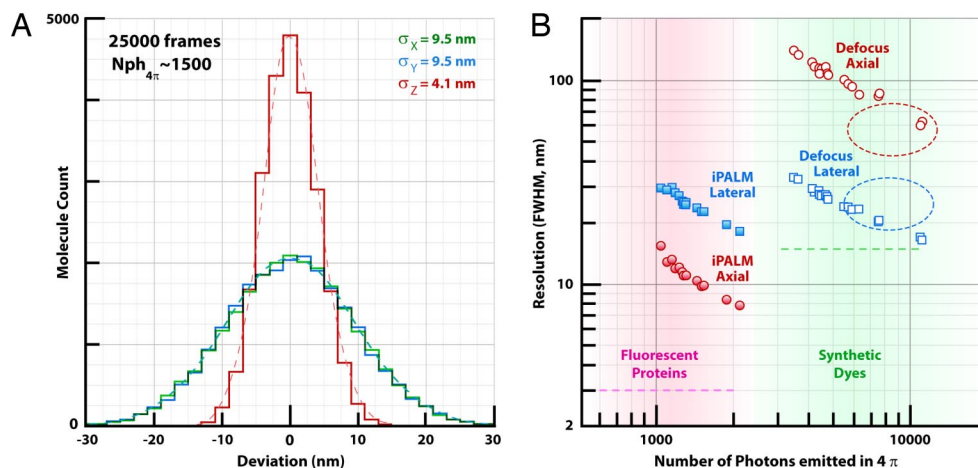


**Fig. 2.** X, Y, Z resolution of iPALM and its dependence on source brightness, illustrating iPALM's sub-20-nm 3D resolution with endogenous FP labels. (A) A histogram of experimentally determined positions from repeatedly sampling (25,000 frames) a source where  $\approx 1,200$  photons are detected per frame from  $\approx 1,500$  photons emitted into a  $4\pi$  solid angle. (B) Axial (solid red circles) and lateral (solid blue squares) resolution of iPALM determined from FWHM of localization of Au beads of different brightness. Note that the positional FWHM number is 2.4 times larger than  $\sigma$  the variance that is also used to characterize resolution. Axial (empty red circles) and lateral (empty blue squares) resolution of the defocusing method determined from FWHM of localized position of Au beads of different brightness. Large ovals indicate approximately the published results for axial (red) and lateral (blue) resolutions of 3D STORM (2) and BP PALM (3). The typical photon output of fluorescent protein tags and synthetic fluorophores are depicted as pink and green gradients. Also shown (horizontal dashed lines) are addition uncertainties resulting from the displacement between the target protein and the fluorescent probes for different imaging methods.

illustrates that iPALM provides 10-fold improvement in axial resolution and 100-fold improvement in photon efficiency compared with the defocus-based techniques (Fig. 2B). Thus, where defocusing methods require antibody-based or cytochemical methods for labeling proteins with brighter organic fluorochromes, iPALM allows accurate localization of FPs even with their modest photon output (typically 500 detected photons for a  $2\pi$  solid angle). In addition to the advantages of a genetically encoded fluorescent label for specificity, the small size of FPs (3–4 nm) compared with antibodies ( $>10$  nm) confers improvements in spatial sampling density and significantly reduces the localization uncertainty because of probe size, which, in the case of antibody, can introduce up to 15 nm in additional FWHM. These additional uncertainties are illustrated by dotted lines in Fig. 2B. An additional benefit of iPALM compared with defocus-based methods is a factor of 2 better lateral resolution because of the factor of 2 (dual objectives) better photon collection efficiency and the optimal image focusing (2, 3).

We demonstrate the 3D superresolution capability of iPALM on fixed cells expressing photoswitchable or photoactivatable FP fusion proteins. The multiphase interferometric microscopy (the *i* in iPALM) recovers the *z*-axis position, and simultaneously PALM (6, 22, 23) recovers the *x*-*y* coordinates on high densities of FP-fusion molecules that occur in cellular structures. Typically,  $>20,000$  frame triplets of individually imaged photoactivatable FPs are acquired, which capture different proteins with 10–100 labeled molecules per frame. In this manner, a compiled list of 100,000–2,000,000 molecular locations can be combined to form the basis for a 3D volume rendering of protein distributions. iPALM thereby achieves 3D protein-specific contrast images at the size scale associated with electron tomography.

To demonstrate the resolution and sensitivity of iPALM, we imaged well-characterized cellular ultrastructure. Electron microscopy has established that microtubules, which serve as a polarized structural scaffold within cells, have a 25 nm diameter (24). Previous fluorescent-based superresolution 3D imaging approaches (2–4) have lacked the resolution to demonstrate this size. With iPALM, we have resolved the diameter of the microtubules to nearly their known dimension along the *z* axis. This is illustrated in the iPALM image Fig. 3 of a PtK1 cell expressing human  $\alpha$ -tubulin

fused to a monomeric variant of the fluorescent protein KikGR (25). The color-coded height image of multiple microtubules crossing each other vertically shows individual microtubules as distinct colors (Fig. 3C). A *z* axis histogram (Fig. 3D) for 2 of the microtubules crossing within 70 nm of each other (boxed region in Fig. 3A) shows a FWHM of 25–30 nm for each microtubule. This size is in good agreement with the dimension of the microtubule itself plus the size of the FP (24). This illustrates the power of iPALM to reveal the 3D morphology with high molecular specificity on a scale

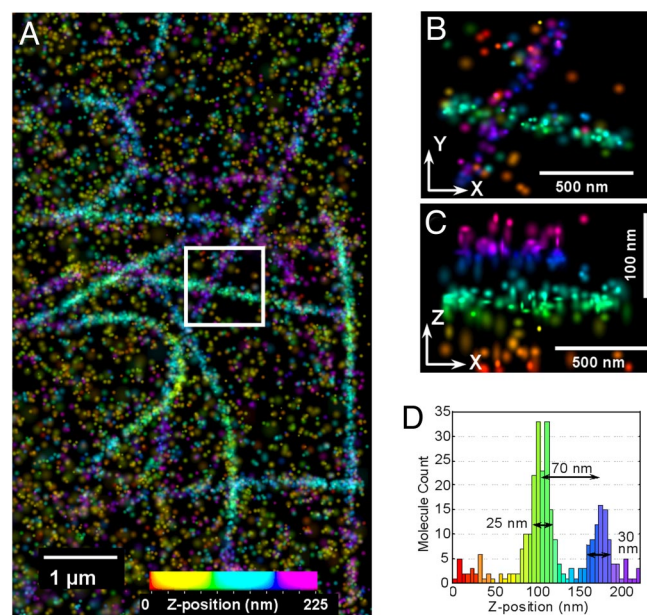


**Fig. 3.** Superresolution iPALM image of microtubules in a PtK1 cell expressing human  $\alpha$ -tubulin fused to *m*-KikGR, rendered with *z* axis color-coding. (A) Large area overview. (B and C) Zoom-in of the area bound by the white box in A. (D) Histogram of *z*-positions of molecules in the boxed region. Each microtubule has a FWHM of 30 nm, and the separation distance of 70 nm between the cyan and purple microtubules is easily resolved.

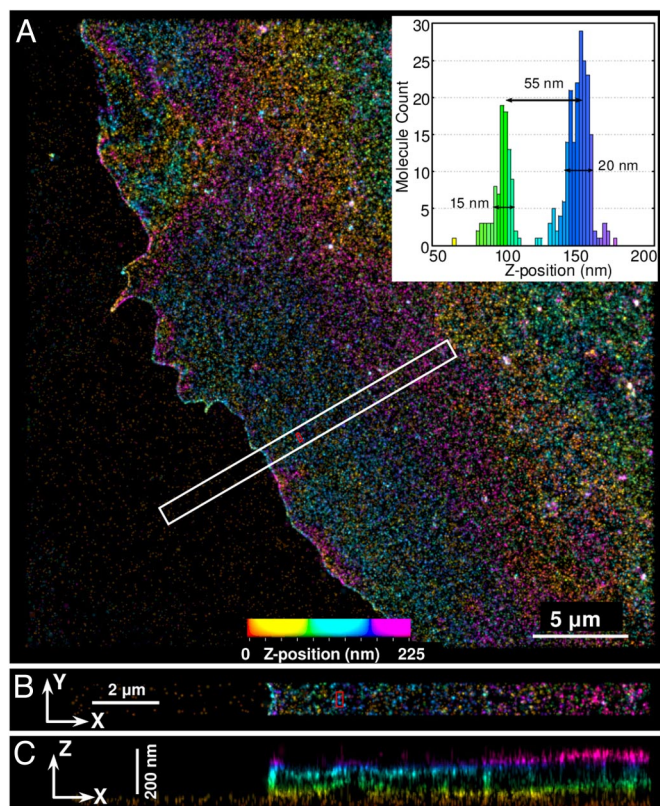


**Fig. 4.** Superresolution iPALM image of COS7 cell expressing the membrane protein VSVG fused to td-EosFP, rendered with z axis color-coding. (A) Large area overview. (B and C) Area outlined in white is enlarged in B and shown in C as a z cross-section. Shown in the *Inset* is the histogram of vertical distribution of fluorescent molecules in the area limited by the red rectangle.

relevant for understanding how these proteins are organized and function with other molecular partners within the cell.

Another class of biological structures where iPALM can provide insights is the plasma membrane system, which serves as the boundary between the cytoplasm and extracellular environment. To visualize the plasma membrane, COS-7 cells were transiently transfected with the transmembrane vesicular stomatitis virus G protein (VSVG) tagged with tandem-dimer-Eos FP (tdEosFP) (26). The vertical position of VSVG molecules in the plasma membrane over a 225-nm range is represented by a color hue scale (Fig. 4). A cross-section of the area bound by the white rectangle separately resolves both the dorsal and ventral plasma membrane, even for spacings  $\approx 60$  nm and shows a cell surface protrusion with an average thickness of 110–160 nm (Fig. 4C), consistent with electron microscopy (27). The lateral dimensions of the displayed area are an order of magnitude wider than the vertical scale so the vertical variations because of membrane roughness manifest as increased apparent membrane thickness in the cross-section. Atomic force microscopy (AFM) measures membrane roughness with the same degree of precision (28), however, with iPALM, we are able to access the topology of the membrane opposing the coverslip with equal precision, which AFM cannot. With the axial resolution provided by iPALM, issues such as plasma membrane polarity and endocytic protein organization can now be investigated at the molecular level.

The molecular precision and spatial resolution of iPALM are especially useful for probing the endomembrane system and its interaction with other cellular structures, particularly in the axial dimension. The 3D mapping of another membrane protein,  $\alpha_v$  integrin fused with tdEos, coexpressed with untagged  $\beta_1$  integrin

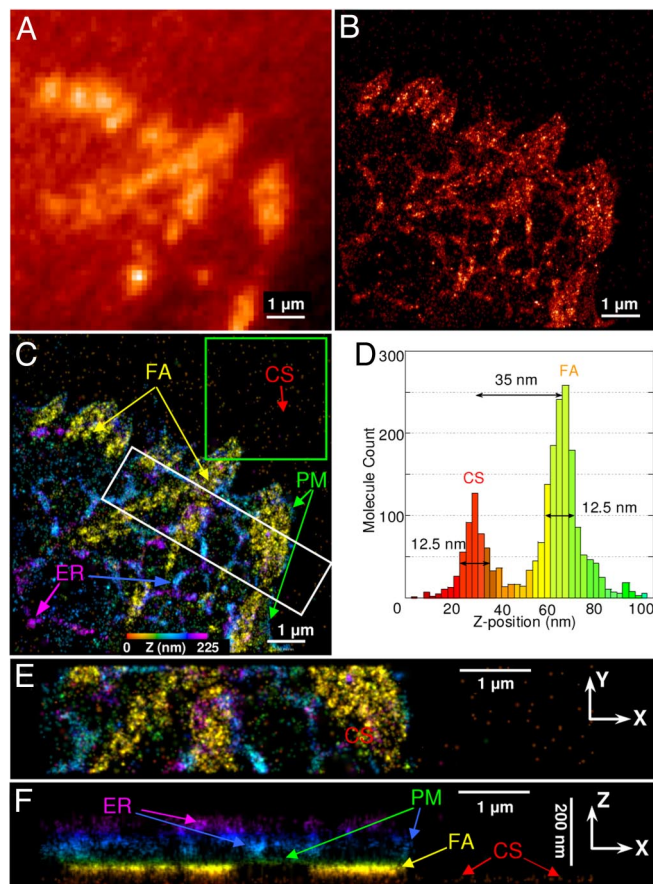


**Fig. 5.** U2OS cell expressing td-EosFP- $\alpha_v$ -integrin. (A–C) Widefield (A) and PALM (B) images, and z color-coded iPALM image (C). The coverslip surface (CS), focal adhesion (FA), cell plasma membrane (PM), and endoplasmic reticulum (ER) can be identified. (D) Z-position histogram of area limited by the green box in C with peaks corresponding to CS and FA. (E and F) X–Y (E) and X–Z (F) projections of the area bound by the white box in C. Z-scale is magnified by 4 in F.

in U2OS cells, demonstrates this capability (Fig. 5). Integrins are  $\alpha\beta$  heterodimeric transplasma-membrane receptors that cluster in the membrane to form focal adhesions (FAs), where they bind to the extra extracellular matrix and serve as mechanical and signaling linkages between the cells and their environment. The iPALM image (Fig. 5C) with color-encoded vertical position clearly identify those integrin  $\alpha_v$  molecules that are incorporated into FAs (yellow in Fig. 5 C, E, and F), whereas a sparser distribution of  $\alpha_v$  integrins outline the contour of the plasma membrane. Furthermore, a network of tubular structures is observed at  $>70$  nm above the coverslip plane, which reveals the endoplasmic reticulum (ER) decorated by newly synthesized  $\alpha_v$  integrin. The iPALM image clearly identifies finger-like ER structures juxtaposing FA, suggestive of their involvement in integrin delivery (see SI for a movie clearly resolving the ER lumen). Within an FA,  $\alpha_v$  integrin occupies a very narrow height distribution of  $<15$ -nm FWHM at a vertical displacement of  $\approx 35$  nm above the coverslip surface, in good agreement with the cell–substratum separation of  $\approx 15$ – $20$  nm, known from electron or interference reflection microscopy (27, 29). Together with the plasma membrane thickness and the position of the tdEos FP tag at the cytoplasmic domain of the integrin  $\alpha_v$ , it is also in agreement with the distance between integrin-based adhesions and coverglass determined by interference reflection microscopy (29). The demonstrated 15-nm precision (FWHM) of vertical localization of FP-tagged integrin illustrates the poten-





the derivations in ref. 19, we obtain the expression for the standard deviation of localization along  $z$  axis:

$$\sigma_z - iPALM = \frac{s_z - iPALM}{\sqrt{N_{tot}}}, \text{ where } s_z - iPALM = \frac{\lambda(1 + NA/8)}{4\pi n}. \quad [7]$$

For aqueous sample medium with  $n \approx 1.33$ ,  $\lambda = 590$  nm, and for  $NA = 1.4$ , Eqs. 5 and 7 give the localization accuracies of  $\sigma_{xy} \approx 100$  nm/ $\sqrt{N_{tot}}$  and  $\sigma_z \approx 40$  nm/ $\sqrt{N_{tot}}$ .

It should be pointed out that the only approximation made in deriving Eq. 7 is the omission of the background noise, so when compared with localization accuracy in  $x$ - $y$  plane it should be compared with the first 2 terms in Eq. 4.

The contribution of the background noise (third term in Eq. 4) scales as  $s^4$ , so its relative contribution is smaller for  $z$  axis localization than that  $x$ - $y$ -plane localization.

Biological samples do have index variations that can give additional phase shifts to the radiating photons that depend on

direction and the optical index along that path. This gives rise to slowly varying (over micron lateral scale) distortions. For example the position of molecules on the coverslip surface appear not flat but bowed down by 2–5 nm under a cell of Fig. 4 or Fig. 5. This results from a higher index cell in a lower index aqueous media. However, a reference plane such as fluorescent layer localized on a glass surface allows one to monitor the error from index changes and offers a reference by which to correct for it.

The details of experimental setup and sample preparation are given in SI.

**ACKNOWLEDGMENTS.** We thank J. Wiedenmann and U. Nienhaus (Ulm University, Ulm, Germany) for the gift of the EosFP, A. Miyawaki (RIKEN, Wako, Saitama, Japan) for the  $m$ -KikGRFP, Patrick Lee for mechanical design of the iPALM, Hari Shroff and Eric Betzig for help and discussions, Ann McEvoy and Derek Greenfield (University of California, Berkeley) for intriguing 3D samples, and Kevin McGowan and Helen White for help with samples. This work was supported by the Howard Hughes Medical Institute and the National Institutes of Health intramural programs of the National Institute of Neurological Disorders and Stroke, the National Institute of Dental and Craniofacial Research, the National Institute of Child Health and Human Development, and the National Heart, Lung, and Blood Institute.

- Gustafsson MGL, et al. (2008) Three-dimensional resolution doubling in wide-field fluorescence microscopy by structured illumination. *Biophys J* 94(12):4957–4970.
- Huang B, Wang WQ, Bates M, Zhuang XW (2008) Three-dimensional super-resolution imaging by stochastic optical reconstruction microscopy. *Science* 319(5864):810–813.
- Juette MF, et al. (2008) Three-dimensional sub-100 nm resolution fluorescence microscopy of thick samples. *Nat Methods* 5(6):527–529.
- Schmidt R, et al. (2008) Spherical nanosized focal spot unravels the interior of cells. *Nat Methods* 5(6):539–544.
- Vaziri A, Tang J, Shroff H, Shank CV (2008) Multilayer 3-dimensional super resolution imaging of thick biological samples. *Proc Natl Acad Sci USA* 105(51):20221–20226.
- Betzig E, et al. (2006) Imaging intracellular fluorescent proteins at nanometer resolution. *Science* 313(5793):1642–1645.
- Hariharan P (2003) *Optical Interferometry* (Academic, Boston), 2nd Ed, p 351.
- Linnik VP (1933) Simple interferometer for the investigation of optical systems. *C R Acad Sci* 1:208–210.
- Delaunay G (1953) Microscope interférentiel A. Mirau pour la mesure du fini des surfaces. *Rev Opt Theor Instrum* 32:610–614.
- Bhushan B, Wyant JC, Koliopoulos CL (1985) Measurement of surface-topography of magnetic tapes by mirau interferometry. *Appl Opt* 24(10):1489–1497.
- Hell S, Stelzer EHK (1992) Fundamental improvement of resolution with a 4pi-confocal fluorescence microscope using 2-photon excitation. *Opt Commun* 93(5–6):277–282.
- Gustafsson MGL, Agard DA, Sedat JW (1995) Sevenfold improvement of axial resolution in 3D widefield microscopy using two objective lenses. *Proc SPIE* 2412:147–156.
- Braun D, Fromherz P (1998) Fluorescence interferometry of neuronal cell adhesion on microstructured silicon. *Phys Rev Lett* 81(23):5241–5244.
- Bilenca A, et al. (2008) Fluorescence interferometry—Principles and applications in biology. *Fluor Methods Appl Spectr Imaging Probes* 1130:68–77.
- Dogan M, et al. (2008) Spectral self-interference fluorescence microscopy for subcellular imaging. *IEEE J Sel Top Quant Electron* 14(1):217–225.
- Poisel H, Trommer G (1990) Optical-fiber gyroscope of sagnac type having a fiber-optic loop and 3×3 coupler. *US Patent* 4,944,590.
- Peale D, Duran C, Hess H (2004) Waveguide based parallel multi-phaseshift interferometry for high speed metrology, optical inspection, and non-contact sensing. *US Patent* 6,687,008.
- Peale DR, Hess H (2008) Evanescent waveguide couplers. *US Patent* 7,333,690.
- Thompson RE, Larson DR, Webb WW (2002) Precise nanometer localization analysis for individual fluorescent probes. *Biophys J* 82(5):2775–2783.
- van Oijen AM, Köhler J, Schmidt J, Müller M, Brakenhoff (1998) GJ 3-Dimensional super-resolution by spectrally selective imaging *Chem Phys Lett* 292(1–2):183–187.
- Pin Kao H, Verkman AS (1994) Tracking of single fluorescent particles in three dimensions: Use of cylindrical optics to encode particle position. *Biophys J* 67(3):1291–1300.
- Hess ST, Girirajan TPK, Mason MD (2006) Ultra-high resolution imaging by fluorescence photoactivation localization microscopy. *Biophys J* 91(11):4258–4272.
- Rust MJ, Bates M, Zhuang X (2006) Sub-diffraction-limit imaging by stochastic optical reconstruction microscopy (STORM). *Nat Methods* 3(10):793–796.
- Osborn M, Webster RE, Weber K (1978) Individual microtubules viewed by immunofluorescence and electron-microscopy in same Ptk2 cell. *J Cell Biol* 77(3):R27–R34.
- Habuchi S, Tsutsui H, Kochaniak AB, Miyawaki A, van Oijen AM (2009) mKikGR, a monomeric photoswitchable fluorescent protein. *PLoS ONE* 3(12).
- Wiedenmann J, et al. (2004) EosFP, a fluorescent marker protein with UV-inducible green-to-red fluorescence conversion. *Proc Natl Acad Sci USA* 101(45):15905–15910.
- Abercrombie M, Heaysman JE, Pegrum SM (1971) The locomotion of fibroblasts in culture. IV. Electron microscopy of the leading lamella. *Exp Cell Res* 67(2):359–367.
- Frankel DJ, et al. (2006) Revealing the topography of cellular membrane domains by combined atomic force microscopy/fluorescence imaging. *Biophys J* 90(7):2404–2413.
- Izzard CS, Lochner LR (1976) Cell-to-substrate contacts in living fibroblasts—Interference reflection study with an evaluation of technique. *J Cell Sci* 21(1):129–159.
- Manley S, et al. (2008) High-density mapping of single-molecule trajectories with photoactivated localization microscopy. *Nat Methods* 5(2):155–157.
- Gouy LG (1890) Sur une propriété nouvelle des ondes lumineuses. *C R Acad Sci* 110:1251–1253.
- Linfort EH, Wolf E (1956) Phase distribution near focus in an aberration-free diffraction image. *Proc Phys Soc B* 69:823–832.
- Miller JE, Brock NJ (2001) Methods and apparatus for splitting, imaging, and measuring wavefronts in interferometry *US Patent* 6,304,330.
- Hecht E (1998) *Optics* (Addison—Wesley, Reading, MA), 3rd Ed, Section 9.6.
- Born M, Wolf E (1984) *Principles of Optics* (Pergamon, Oxford), 6th Ed, Section 8.5.2.

# Supporting Information

Shtengel et al. 10.1073/pnas.0813131106

## SI Text

**Demonstration of iPALM Resolution.** An example of the 3 interference images of sparsely distributed fluorescent fiducials (100-nm Au particles chosen for 561-nm excitation and stability over the course of the experiment) at a specific  $z$  height is shown in Fig. S1A. These fiducials serve 3 purposes: to calibrate and align the system, to track any nanometer scale sample drift so that it can be corrected, and to demonstrate localization accuracy. If the sample is translated along the  $z$  axis, then the intensities cycle among the 3 cameras. Typically, we capture 800–1,200 photons total across all 3 cameras per frame for a single fiducial. A plot of the intensity vs.  $z$  position for a typical fiducial is shown in Fig. S1B. Using Eq. 3, a  $z$  position can be extracted for each 3-element intensity vector. The  $z$  positions derived from the intensities for all fiducials (within field of  $20 \times 20 \mu\text{m}$ ) imaged over a range of displacements is shown in Fig. S1C and demonstrates uniform sensitivity.

The observed spread of vertical locations within each frame is most likely dominated by variations in the fiducial heights across the field. Notice that the position can be determined uniquely in a 225-nm range which defines a preferred sample thickness. Thicker samples can be accommodated by incorporating an independent technique such as defocused PSF or the degree of coherence to determine the order of the interference fringe, an integer multiple of 225 nm.

One can test the variance in localization for a hypothetical source where  $\approx 1,000$  photons are captured, a value typical for a FP. This is emulated by repeatedly sampling (25,000 frames) a typical fiducial so that only 1,000–1,200 photons are captured per 50-ms sampling, and  $x$ ,  $y$ , and  $z$  coordinates are calculated based on the data. A histogram of the position in Fig. 2A shows a variance of  $\sigma_{xy} = 9.5$  nm laterally and a more precise  $\sigma_z = 4.1$  nm using interferometry. The ratio  $\sigma_z/\sigma_{xy} \approx 0.43$  observed here is very close to the value of 0.40 obtained analytically from Eqs. 5 and 7.

**Experimental Setup.** The experimental setup is shown schematically in Fig. 1A. The samples in study were sandwiched between 2 #1.5 coverslips (Warner Instruments). This assembly was placed between 2 opposing infinity-corrected microscope objectives (Nikon CFI Apochromat TIRF 60 $\times$ ,  $NA = 1.49$ , Nikon); index matching oil was used (Cargille type DF; Cargille Laboratories). We used the light from a 50-mW diode laser at  $\lambda_{\text{act}} = 405$  nm (Coherent Inc.) for activation of the fluorescent proteins, and 150 mW,  $\lambda_{\text{exc}} = 561$  nm diode pumped solid-state laser (CrystaLaser) for excitation of activated fluorescent proteins. Narrow-bandwidth laser line filters (MaxLine LL01–561–12.5 and MaxDiode LD01–405/10–12.5; Semrock Inc.) were used to reject both emission noise from the laser and autofluorescence generated in the optical path before the objectives. The activation and excitation beams entered the back pupil planes of the objectives through the slots in the custom turning mirrors (Reynard Corp.). The radial position of these beams was controlled to produce near-total internal reflection (TIR) condition. The fluorescence signal was collected by the infinity-corrected objectives and the image-forming beams were interfered in the 3-way beam splitter custom manufactured by Rocky Mountain Instruments. The output beams from 3-way beam splitter were then focused on 3 separate EMCCD cameras (Andor iXon DU-897; Andor Technology) via  $f = 400$ -mm achromatic lenses (01LAO799; CVI Melles Griot). To reject the excitation light from registration, we used the long-pass and band-pass optical

filters (RazorEdge LP02–633RU-25 and BrightLine FF01–588/21–25; Semrock Inc.). A typical measurement consisted of 20,000–100,000 frame triplets with excitation/collection exposure time of 50 ms, and the 5- to 30-ms activation pulses were transmitted between the excitation pulses.

**Sample Preparation. Coverslip preparation.** First, the 18- and 25-mm #1.5 coverslips (Warner Instruments) were cleaned by immersion for at least 2–3 h in stirred solution at 85 °C of 5:1:1  $\text{H}_2\text{O}/\text{H}_2\text{O}_2$  (50%; Fisher Scientific)/ $\text{NH}_4\text{OH}$  (100%; Fisher Scientific).

After cleaning, 50  $\mu\text{l}$  of 0.1% PolyL-Lysine (Ted Pella) was deposited on the top surface of the 18-mm coverslips and incubated for 30 min. The coverslips were then rinsed with  $\text{H}_2\text{O}$  and blow-dried with purified air.

After this, 50  $\mu\text{l}$  of 5% (1:20 diluted in  $\text{H}_2\text{O}$ ) Au 100-nm beads (100-nm Gold nanospheres 5.6E9 per ml, 20 ml; Microspheres-Nanospheres) was deposited on the top surface of 18-mm coverslips and incubated for 5 min. The coverslips were then rinsed with  $\text{H}_2\text{O}$  and blow-dried with purified air.

Finally, 50 nm of  $\text{SiO}_2$  was deposited on the top surface of the 18-mm coverslips using Gatan 682 Precision Etching Coating System (Gatan) and cleaned again in the solution described above.

The cells were then grown on the top surface of the 18-mm coverslips. After fixation, the clean 25-mm coverslip was placed above the cells and sealed using 5-min epoxy (ITW Performance Polymers) and Vaseline (Unilever).

**Mammalian expression vectors.** All expression vectors were constructed using C1 and N1 (Clontech-style) cloning vectors. tdEos cloning vectors were prepared as previously described (1). A bacterial vector containing the coding sequence for mKikGR was amplified with a 5' primer encoding an AgeI site and a 3' primer encoding either a BspEI (C1) or NotI (N1) site. The purified and digested PCR products were ligated into similarly digested EGFP-C1 and EGFP-N1 cloning vector backbones. To generate fusion vectors, the appropriate cloning vector and an EGFP fusion vector were digested, either sequentially or doubly, with the appropriate enzymes and ligated together after gel purification. Thus, to prepare mKikGR- $\alpha$ -tubulin the following digest was performed: NheI and BglII (EGFP- $\alpha$ -tubulin; Clontech), and to prepare tdEos- $\alpha$ -v-integrin the following digest was performed: AgeI and NotI (Waterman Lab Clontech-style N1-EGFP- $\alpha$ -v-integrin). DNA for mammalian transfection was prepared using the Plasmid Maxi kit (Qiagen). Vectors were verified by sequencing (FSU Biological Science Sequencing Facility) and were expressed in HeLa cells to confirm localization (Figs. S2 and S3).

To prepare the VSVGtsO45-NL-tdEosFP, the VSVGtsO45-NL-encoding DNA was removed from the VSVGtsO45-NL-tdEosFP plasmid (previously described in ref. 2) by restriction endonuclease digestion using XhoI and BamHI and ligated into a similarly digested tdEosFP-N1 plasmid.

**Cell culture and transfection.** PtK1 (Potoroo kidney) cells (ATCC) (Fig. 3) were cultured in Phenol-red free DMEM-F12 supplemented with 10% FBS and 2 mM glutamine (Invitrogen). Cells were trypsinized by 0.25% trypsin/EDTA (Invitrogen), counted, pelleted, and resuspended in Nucleofector Solution R (Amaxa). Approximately  $1 \times 10^6$  cells were mixed with 5  $\mu\text{g}$  of mKikGR-tubulin and electroporated according to Amaxa Nucleofector protocol A-023.

Electroporated cells were plated onto iPALM coverslips that

had been washed for 1 h at 70 °C in 5:1:1 solution of H<sub>2</sub>O/H<sub>2</sub>O<sub>2</sub>/NH<sub>4</sub>OH (see *Coverslip preparation*), washed in acetone, dried, baked at 120 °C for 1 h, then silanized with vapor phase HMDS (Hexamethyldisilazane; Sigma–Aldrich) as previously described (3), and then coated with 7.5 µg/ml human fibronectin (Chemicon) at 4 °C overnight. Coverslips were rinsed with supplemented media before the addition of electroporated cells.

COS7 (African green monkey kidney) cells (Fig. 4) were cultured in RPMI medium 1640 supplemented with 10% FBS, 100 mM sodium pyruvate, 100× non-essential amino acids, 100× MEM vitamin solution, 7.5% sodium bicarbonate solution, and 100 units/ml of penicillin/streptomycin (Invitrogen). Cells were trypsinized by 0.05% Trypsin/EDTA (Invitrogen) and cultured on iPALM coverslips 24 h before transfection. Cells were transfected using the Fugene 6 Reagent (Roche) according to manufacturer's protocol with a ratio of 3 µl of Fugene per 2 µg of VSVGtsO45-NL-tdEosFP DNA and fixed ≈24 h after transfection.

U2OS (human osteosarcoma) cells (Fig. 5) were cultured in McCoy5A media supplemented with 10% FBS, 2 mM glutamine, and 100 units/ml penicillin/streptomycin (Invitrogen). Cells were grown for 2 days and trypsinized by 0.25% Trypsin/EDTA (Invitrogen), counted, pelleted, and resuspended in Nucleofector Solution V (Amaxa). Approximately 1 × 10<sup>6</sup> cells were mixed with 1 µg each of DNA vectors for tdEosFP-tagged α<sub>v</sub>-integrin

and untagged β<sub>1</sub>-integrin (to aid in proper localization of the integrin αβ heterodimer, obtained as a kind gift from Mark Ginsberg (University of California, San Diego, School of Medicine). Electroporation of the suspended cells were carried out using Amaxa nucleofector program X-001 per manufacturer's protocol. Electroporated cells were then directly transferred to 18-mm iPALM coverslips in a 6-well tissue culture plate. Phenol red-free McCoy5A media (HyClone) similarly supplemented, was used at this stage of culture to minimize any potential contaminating fluorescence from phenol red dyes.

To prepare for cell growth, iPALM coverslips were briefly rinsed with Dulbecco's phosphate buffered saline (DPBS; Invitrogen), and incubated with 10 µg/ml human plasma fibronectin (FC010–5MG; Chemicon International) at 4 °C overnight. Coverslips were then rinsed with DPBS and incubated with 1% heat-inactivated BSA (A3059; Sigma) for 1 h at 37 °C before a final rinse with DPBS.

**Cell fixation.** COS7 and PtK1 cells were treated with 10 nM taxol for 20–30 min at 37 °C before fixation to stabilize microtubules. All cells were fixed with either 2% paraformaldehyde (U2OS) or 2% paraformaldehyde and 0.05% glutaraldehyde (COS7 and PTK1) in PHEM buffer [60 mM Pipes, 25 mM Hepes, 10 mM EGTA, 2 mM MgSO<sub>4</sub> (pH 7.0)] at 37 °C for 10–15 min as previously described (4). All cells were stored in PHEM until imaged.

1. Shroff H, et al. (2007) Dual-color superresolution imaging of genetically expressed probes within individual adhesion complexes. *Proc Natl Acad Sci USA* 104(51):20308–20313.
2. Wiedenmann J, et al. (2004) EosFP, a fluorescent marker protein with UV-inducible green-to-red fluorescence conversion. *Proc Natl Acad Sci USA* 101(45):15905–15910.

3. Regen CM, Horwitz AF (1992) Dynamics of beta(1) integrin-mediated adhesive contacts in motile fibroblasts. *J Cell Biol* 119(5):1347–1359.
4. Galbraith CG, Skalak R, Chien S (1998) Shear stress induces spatial reorganization of the endothelial cell cytoskeleton. *Cell Motil Cytoskeleton* 40(4):317–330.



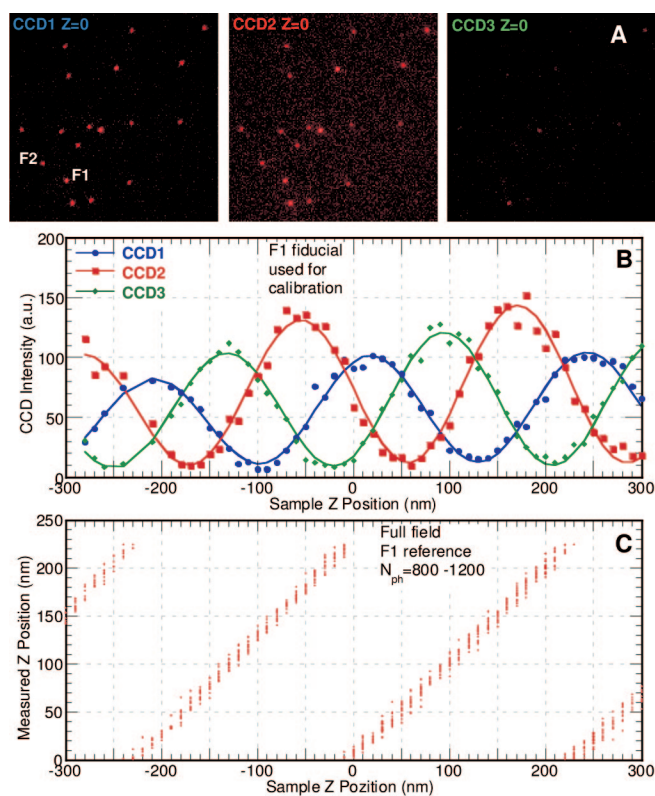


**Fig. S1.** Demonstration of interference on 3 cameras of reference fluorescent fiducials and resulting extracted z position. (A) Three different phase-interfered images of fiducials (100-nm Au particles). (B) The intensity oscillations of fiducial F2 for each of the 3 cameras as its vertical position is varied. (C) The extracted z position based the intensity triplet for all fiducials present in the image.

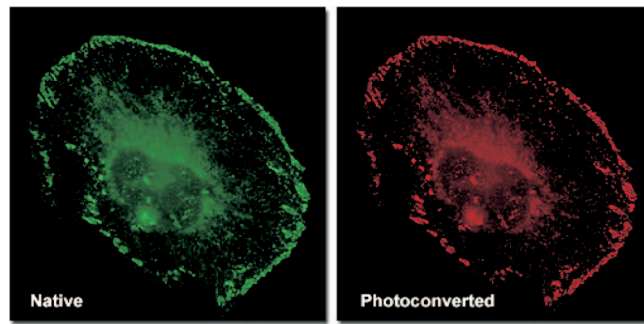


Fig. S2. tdEos- $\alpha_V$ -Integrin in HeLa cells.

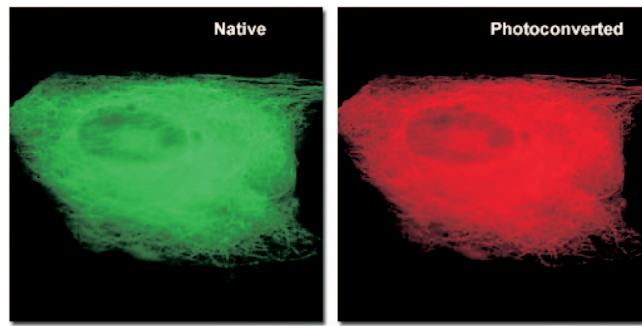
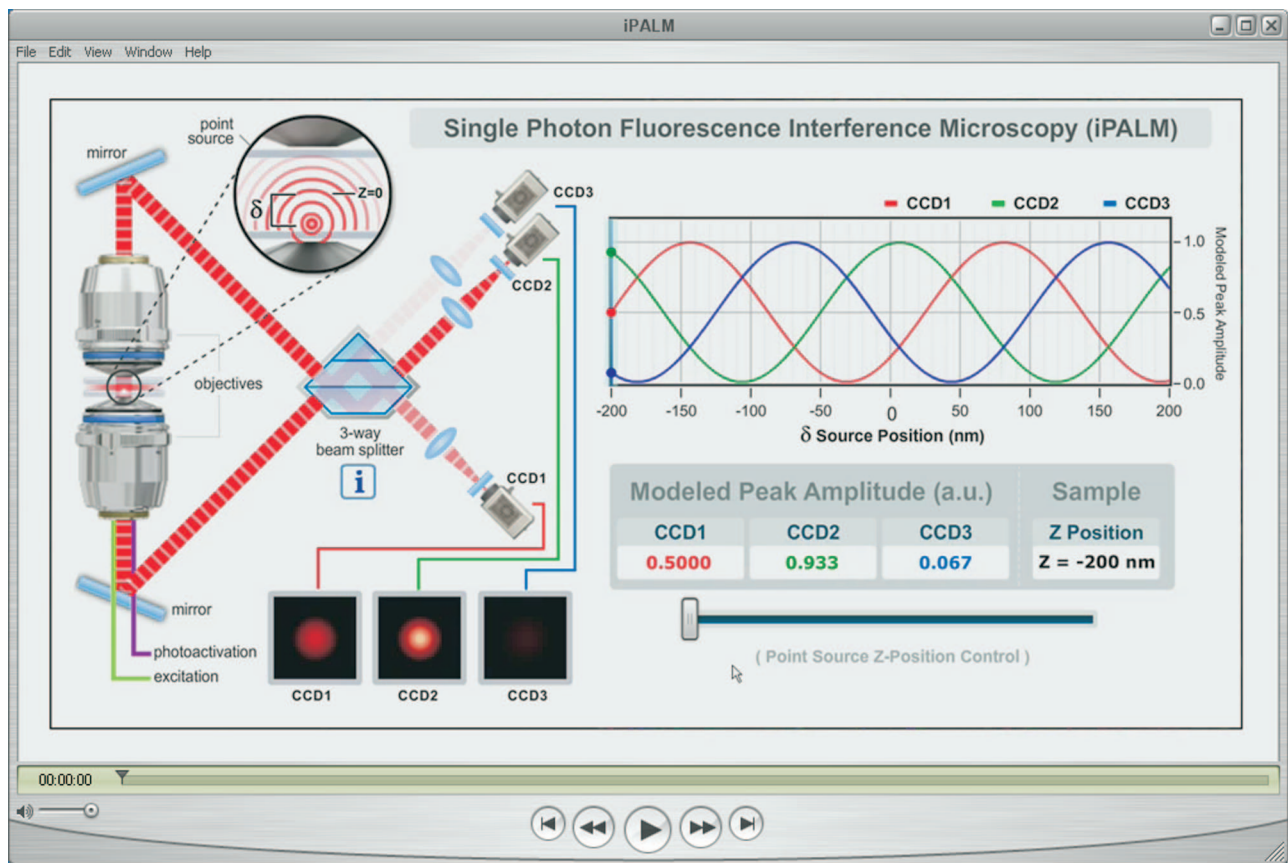


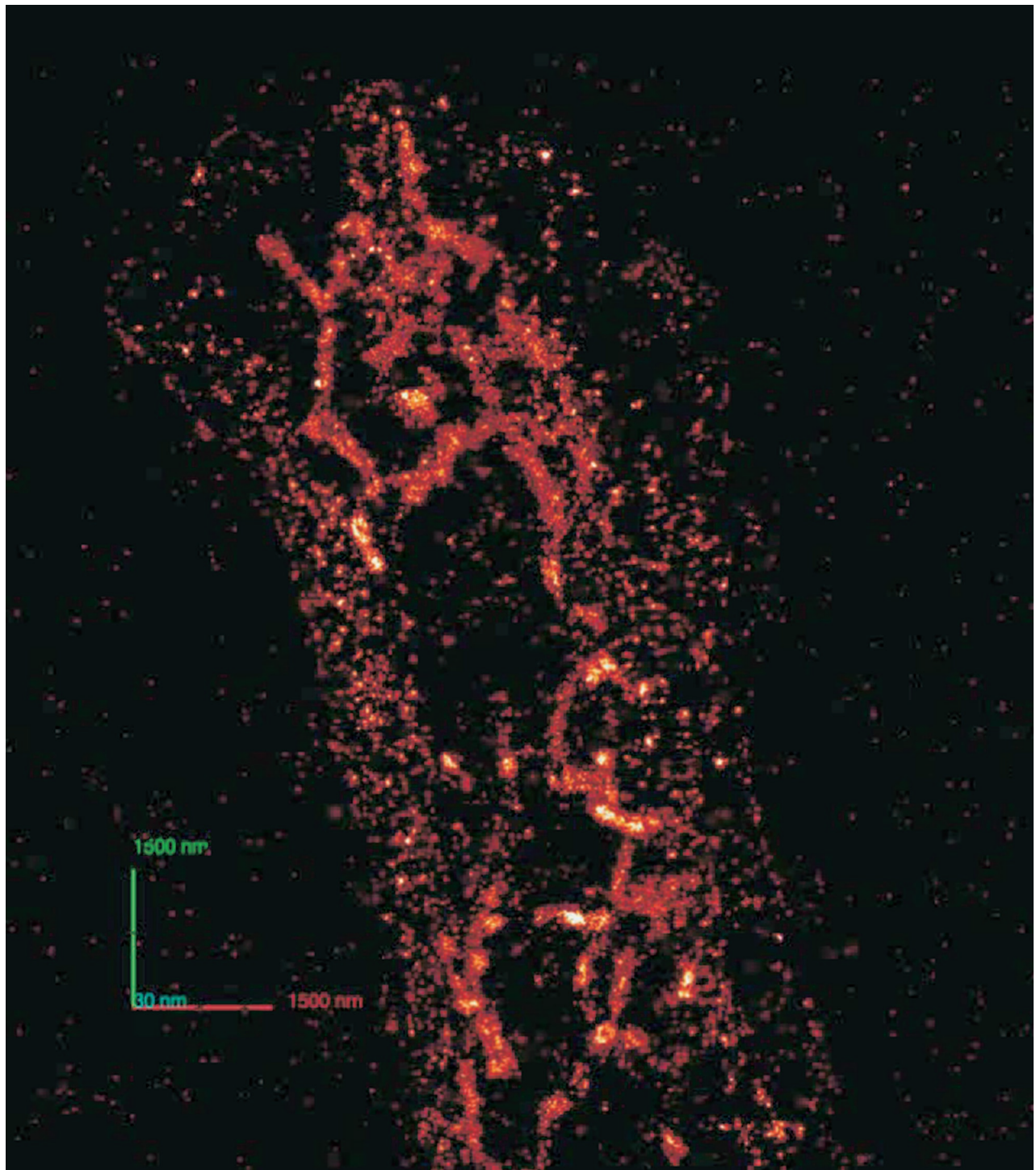
Fig. S3. mKikGR in HeLa cells.





**Movie S1.** iPALM tutorial, illustrating and dependence of the relative intensity of the interferometric image in 3 cameras on the vertical position of the fluorescent source.

[Movie S1 \(MOV\)](#)



**Movie S2.** iPALM-based 3D movie rendering of td-EosFP- $\alpha_v$ -integrin positions inside U2OS cell.

[Movie S2 \(MOV\)](#)